Coherent streamflow variability in Monsoon Asia over the past eight centuries—links to oceanic drivers

Hung T.T. Nguyen[1], Sean W.D. Turner[2], Brendan M. Buckley[3], and Stefano Galelli[1]

[1]Pillar of Engineering Systems and Design, Singapore University of Technology and Design, Singapore
[2]Pacific Northwest National Laboratory, Washington, USA
[3]Lamont-Doherty Earth Observatory, Columbia University, New York, USA

Key Points:

- Climate-informed dynamic streamflow reconstruction is skillful over most of Monsoon Asia
- Streamflow in Monsoon Asia is spatially coherent
- Reconstruction reveals spatial and temporal variability in streamflow–ocean teleconnections

Corresponding author: Hung Nguyen, tanthaihung_nguyen@mymail.sutd.edu.sg

Abstract

The Monsoon Asia region is home to ten of the world's biggest rivers, supporting the lives of 1.7 billion people who rely on streamflow for water, energy, and food. Yet, a synthesized understanding of multi-centennial streamflow variability for this region is lacking. To fill this gap, we produce the first large scale streamflow reconstruction over Monsoon Asia (62 stations in 16 countries, 813 years of mean annual flow). In making this reconstruction, we develop a novel, automated, climate-informed, and dynamic reconstruction framework that is skillful over most of the region. We show that streamflow in Monsoon Asia is spatially coherent, owing to common drivers from the Pacific, Indian, and Atlantic Oceans. We also show how these oceanic teleconnections change over space and time. By characterizing past and present hydroclimatic variability, we provide a platform for assessing the impact of future climatic changes and informing water management decisions.

Plain Language Summary

Ten of the world's biggest rivers are located entirely within the Asian Monsoon region. They provide water, energy, and food for 1.7 billion people. To manage these critical resources, we need a better understanding of river discharge—how does it change over a long time? Are there common variation patterns among rivers? To answer these questions, we use information derived from tree rings to reconstruct average annual river discharge history at 62 gauges in 16 Asian countries. Our reconstruction reveals the riparian footprint of megadroughts and large volcanic eruptions over the past eight centuries. We show that simultaneous droughts and pluvials have often occurred at adjacent river basins in the past, because Asian rivers share common influences from the Pacific, Indian, and Atlantic Oceans. We also show how these oceanic teleconnections change over space and time. Our findings can inform big decisions made on water-dependent infrastructure, thus benefiting the riparian people of the Asian Monsoon region.

1 Introduction

Of the world's 30 biggest rivers, ten are located within Monsoon Asia, and two others originate from this region (Figure 1). These river basins are home to 1.7 billion people (Best, 2019). With high population densities, even smaller basins support the livelihood of millions—e.g., Chao Phraya (Thailand): 25 million, Angat (the Philippines): 13 million, and Citarum (Indonesia): 10 million (Nguyen & Galelli, 2018; Libisch-Lehner et al., 2019; D'Arrigo et al., 2011). River discharge, or *streamflow*, provides water for domestic and industrial uses, irrigation, and hydropower. It sustains aquatic life (including fish yield), carries sediment and nutrients, helps prevent salinization of river deltas, and facilitates navigation. Streamflow is an important link in both the water-energy-food nexus and the ecological cycle. To manage this resource, we need a good understanding of hydrologic variability. Such understanding is often derived from streamflow measurements; however, these instrumental data span typically only a few decades, too short to capture long-term variability and changes in streamflow.

When compared against instrumental data, longer streamflow records reconstructed from climate proxies—such as tree rings—often reveal striking insights. A reconstructed pre-dam variability of the Yellow River (Li et al., 2019) shows that streamflow in 1968–2010 was only half of what should have been; in other words, human withdrawals for agriculture, industry, and municipalities reduced streamflow by half. A reconstruction of the Citarum River (Indonesia) (D'Arrigo et al., 2011) shows that the period 1963–2006 contained an increasing trend of low flow years but no trend in high flow years, compared with the previous three centuries. This finding suggests that 10 million inhabitants of Jakarta may be facing higher drought risks than what is perceived from the instrumental record. The Mongolian "Breadbasket", an agricultural region in north-central Mongolia (Pederson et al., 2013), experienced an unusually wet twentieth-century, and the recent dry epoch is not rare in the last four centuries (Davi et al., 2006; Pederson et al., 2013; Davi et al., 2013). Consequently, agricultural planning cannot take the twentieth century to be the norm, lest history repeats the lesson of the Colorado River Basin: observations over abnormally wet years (Stockton & Jacoby, 1976; Woodhouse et al., 2006; Robeson et al., 2020) led to water rights over-allocation, and the Colorado no longer reaches the Pacific Ocean.

The case of the Colorado River demonstrates that streamflow reconstructions can improve our understanding of water resources availability. Furthermore, with longer streamflow records, low frequency variations of streamflow can be revealed, the frequency and magnitude of floods and droughts can be better quantified, and the risks associated with these natural disasters can be better assessed. These benefits have been demonstrated in Australia (Allen et al., 2017; Tozer et al., 2018), the United States (DeRose et al., 2015; Stagge et al., 2018), Canada (Hart et al., 2010; Sauchyn et al., 2015) and other countries (Lara et al., 2015; Güner et al., 2017). Streamflow reconstructions have also been used to generate stochastic time series for water management applications (Prairie et al., 2008; Sauchyn & Ilich, 2017). These benefits, if realized in Monsoon Asia, can improve the lives of many people, given the dense populations that inhabit river basins in this region.

Compelling evidence calls for more streamflow reconstructions in Monsoon Asia. Tremendous efforts, particularly in the last four years (Figure S1), have partly addressed this need, but the hydrological knowledge gained was limited to individual catchments, more than half of which are in China (Figure S1 and Table S1). A regional, synthesized understanding is lacking. Here, we produce the first large-scale streamflow reconstruction for Monsoon Asia, covering 62 stations in 16 countries, unraveling eight centuries of annual streamflow variability. To achieve this task, we develop a novel automated framework with three main components: (1) a climate-informed proxy selection procedure, (2) a dynamic state-space reconstruction model, and (3) a rigorous cross-validation routine for parameter tuning to achieve optimal skills. We also use the Monsoon Asia Drought Atlas version 2 as the paleoclimatic proxy instead of a tree ring network, as the former offers computational advantages (supported with strong physical and statistical foundations) for this large-scale reconstruction. With this work, 58 stations are reconstructed for the first time while the other four (Citarum, Yeruu, Ping, and Indus Rivers) are extended back in time compared to previous works (D'Arrigo et al., 2011; Pederson et al., 2013; Nguyen & Galelli, 2018; Rao et al., 2018). This data set allows us to assess both local historical water availability and regional streamflow patterns, revealing the spatial coherence of streamflow and its links to the oceans. This understanding may improve the management of river basins and other water-dependent resources.

2 Data

2.1 Streamflow Data

Our reconstruction target is the mean annual flow, and we used the calendar year (January to December) as there is not a common water year across Monsoon Asia (Knoben et al., 2018). We obtained streamflow data from the Global Streamflow Indices and Metadata Archive (GSIM) (Do et al., 2018; Gudmundsson et al., 2018), using stations having at least 41 years of data, and with less than 3% missing daily values. We also received streamflow data from our colleagues for some countries where public streamflow records are not available (see Acknowledgment). Small catchments may be influenced by local conditions more than by broad climate inputs that are captured in the regional paleoclimate proxies (Strange et al., 2019). Therefore, we used only stations where the mean annual flow over the whole time series is at least 50 m^3/s; this threshold is heuristic, and somewhat arbitrary. Details of this initial selection step are provided in Text S2 and in the code repository for this paper (`ntthung.github.com/paleo-asia`, DOI: `10.5281/zenodo.3818117`.)

Many stations in our collection have upstream reservoirs that may interfere with the proxy-streamflow relationship. This interference is stronger for seasonal streamflow than annual streamflow: reservoirs transfer water from the wet season to the dry season, but not all reservoirs retain water from year to year. Reservoirs that are filled and emptied within a year do not change the annual water budget downstream. To minimize reservoir interference, we reconstructed annual streamflow, and we removed stations that have upstream retention times longer than a year. We identified upstream reservoirs by

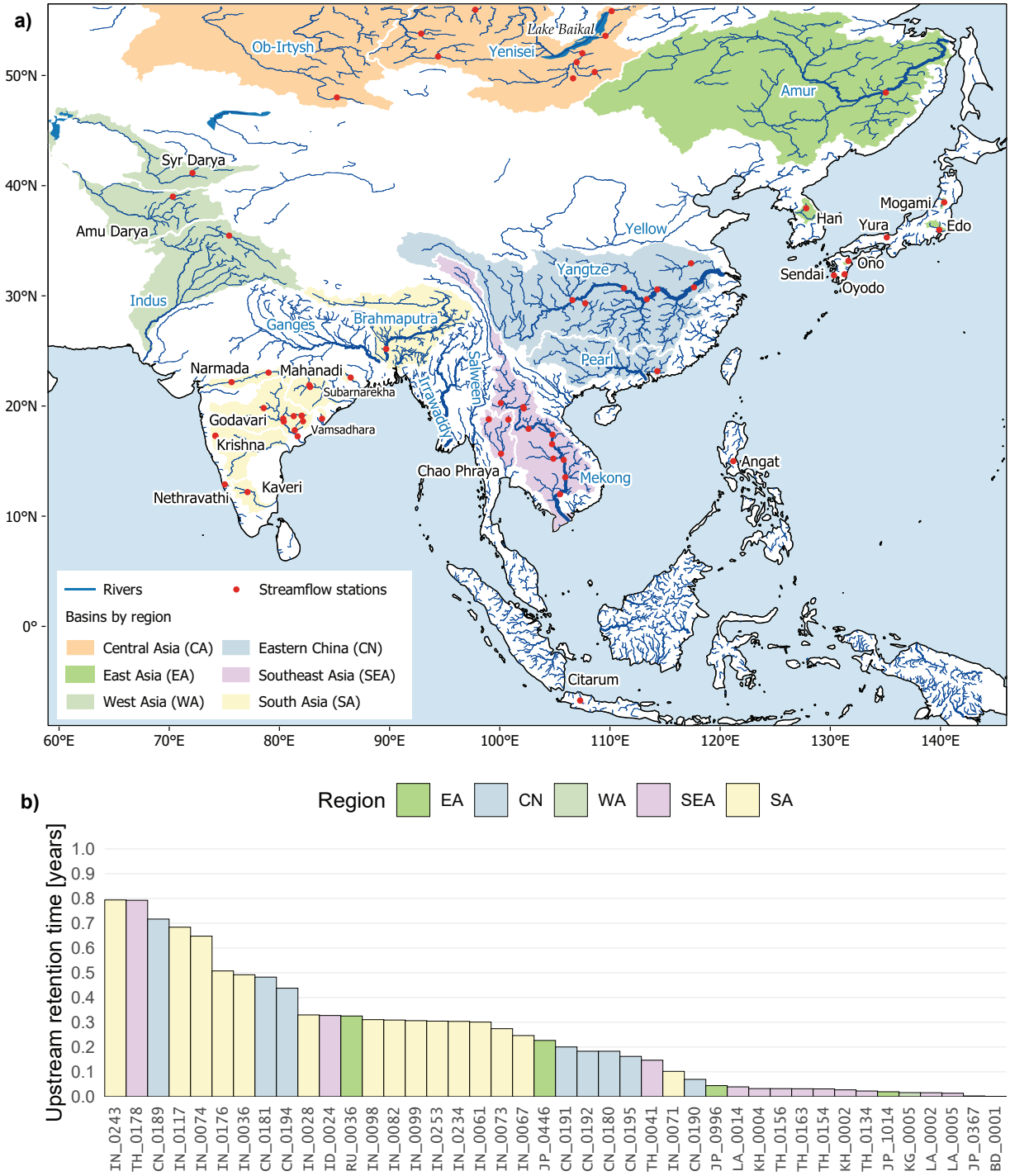

Figure 1. a) The Monsoon Asia region (Cook et al., 2010); river basins involved in this study are highlighted by sub-region, rivers belonging to the world's 30 biggest (Best, 2019) shown with blue names. b) Upstream retention time of the 42 stations that have upstream reservoirs. The bar colours denote the regions according to a). The first two letters of each station's code indicates the country it is in. Refer to Table S2 for station details.

overlaying the Global Reservoirs and Dams (GRanD) data (Lehner et al., 2011) on the river network (Lehner & Grill, 2013; Barbarossa et al., 2018). The upstream retention time was calculated as the total upstream reservoir capacity (million m^3) divided by the mean annual flow volume (million m^3/year). For stations having over-year reservoirs constructed towards the end of their records, we also truncated the corresponding years, keeping only the streamflow data before dam construction.

Our collection and quality control effort resulted in an annual streamflow data set of 62 stations in 16 countries. Our records span across Monsoon Asia, covering the following sub-regions: Central Asia (CA), East Asia (EA), eastern China (CN), West Asia (WA), Southeast Asia (SEA), and South Asia (SA). The stations' locations and upstream retention times (for those having upstream reservoirs) are shown in Figure 1.

2.2 Proxy Data

Our paleoclimate proxy is the Monsoon Asia Drought Atlas version 2 (MADA v2) (Cook, 2015), built upon the original MADA of Cook et al. (2010). The MADA is a gridded data set of the Palmer Drought Severity Index (PDSI) (W. C. Palmer, 1965) over the Asian monsoon region; each grid cell contains an annual time series of the mean June-July-August PDSI, reconstructed from tree rings, and calibrated with the instrumental data set of Dai et al. (2004). The MADA proves to be a reliable long-term record of monsoon strength, having revealed the spatiotemporal extents of the four Asian megadroughts in the last millennium, and linking variations in monsoon strength to sea surface temperature patterns. MADA v2 improves over its predecessor by incorporating more tree ring chronologies (453 versus 327), and targeting the self-calibrating PDSI (scPDSI), which addresses several limitations of the standard PDSI (Wells et al., 2004; van der Schrier et al., 2013). We use the MADA v2 portion between 1200–2012 as this is the common period of most grid points in the atlas (Figure S4), and is also the stable portion with sufficient number of tree ring chronologies in the source tree ring network.

Drought atlases reconstructed from tree rings have been shown to be practical paleoclimate proxies for streamflow reconstruction. Earlier experiments used individual grid points to reconstruct streamflow, either in combination with ring widths (Coulthard et al., 2016) or on their own (Graham & Hughes, 2007; Adams et al., 2015). Ho et al. (2016, 2017), and Nguyen and Galelli (2018) then formalized the methodology and provided theoretical considerations. They reasoned that since both streamflow and PDSI can be modeled as functions of ring width, one can also build a model to relate streamflow to PDSI. Moreover, drought atlases enhance the spatial expression of the underlying tree ring data—by incorporating the modern PDSI field in its calibration—and are also more uniform in space and time than the tree ring network itself (see Cook et al., 2010, Figure 1), making them better suited to large-scale studies. We now elaborate these points as we describe the reconstruction framework.

3 Reconstruction Framework

3.1 Using a Drought Atlas as Paleoclimate Proxy

3.1.1 Physical basis

The main physical processes that involve climate and tree growth are depicted in Figure 2a. The climate at a given location can be characterized by precipitation and temperature, among others. These climatic inputs control soil moisture on land. Except for losses (such as groundwater recharge, evaporation, and surface runoff), the net soil moisture storage then follows two main paths: one goes out of the catchment as streamflow, the other is taken up by the trees and transpired back into the atmosphere, influencing tree growth along the way. Thus, tree growth and streamflow are connected via land-atmosphere interactions—this is the basis for streamflow reconstruction from tree rings (cf. Rao et al., 2018; Li et al., 2019). Note, however, that tree growth does not directly control streamflow, and neither does streamflow control tree growth; we can infer a relationship between them only because they are both influenced by soil moisture. On the other hand, soil moisture directly controls streamflow and is, in principle, a reasonable predictor for streamflow.

It would thus be ideal to have a "natural" soil moisture proxy record, but of course that is not the case. We can instead rely on a surrogate—a soil moisture record reconstructed from tree rings, such as the MADA.

3.1.2 Statistical basis

The physical discussion above yields three types of paleoclimate reconstruction: streamflow from tree rings, soil moisture from streamflow, and streamflow from soil moisture. We now derive mathematically the relationships between these reconstruction types.

Each reconstruction is a conditional distribution of one variable (e.g. streamflow) given that we have observed another variable (e.g. soil moisture), and given the historical climate. We represent these conditional distributions with a probabilistic graphical model (Koller & Friedman, 2009) as shown in Figure 2b. There are four random variables involved: climate (C), soil moisture (S), ring width (R), and streamflow (Q). Each of these variables can be multivariate, i.e., C includes precipitation and temperature, among others, and all variables can include multiple sites or grid points. As a convention, let $f_X(x)$ be the probability density function (PDF) of the random variable X, $f_{XY}(x, y)$ be the joint PDF of X and Y, and $f_{X|Y}(x|y)$ be the conditional PDF of X given that $Y = y$.

Reconstructing streamflow from tree rings is essentially deriving the distribution of Q given R and C, i.e, $f_{Q|R,C}(q|r, c)$, where r is the measured ring width index, and c is the historical climate. We can decompose this distribution as follows:

$$\begin{aligned} f_{Q|R,C}(q|r,c) &= \int f_{Q,S|R,C}(q,s|r,c)\,ds \\ &= \int f_{Q|S,R,C}(q|s,r,c) f_{S|R,C}(s|r,c)\,ds. \end{aligned} \tag{1}$$

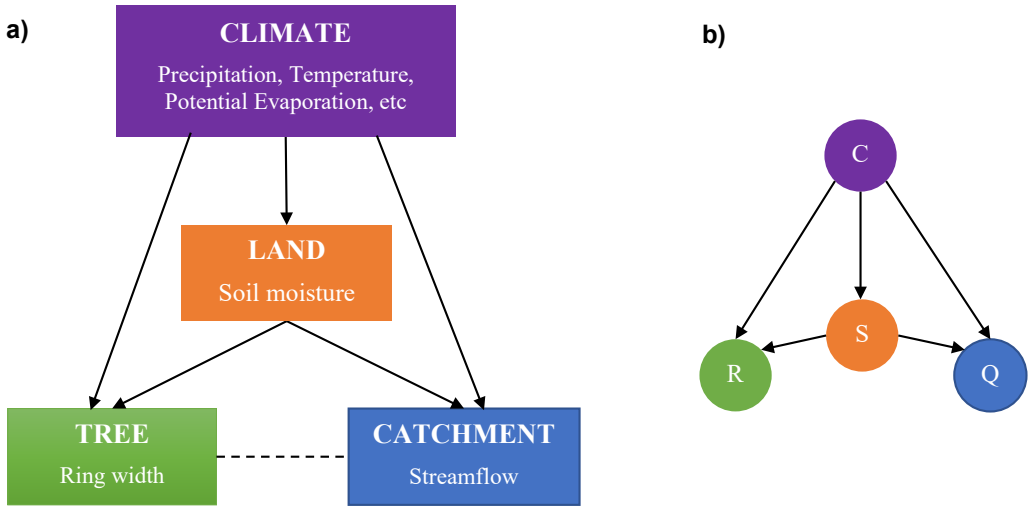

Figure 2. a) Relationships between hydroclimatic variables and tree growth. b) A probabilistic graphical model representing the relationships in a), where C is a vector of climate variables, S the soil moisture, R the ring width index, and Q streamflow. The arrows represent the conditional dependence among variables.

The first equality comes from the relationship between marginal and joint distributions. The second equality comes from Bayes' theorem. Now, Q is independent of R given S and C (Figure 2b), so $f_{Q|S,R,C}(q|s,r,c) = f_{Q|S,C}(q|s,c)$. Consequently,

$$f_{Q|R,C}(q|r,c) = \int f_{Q|S,C}(q|s,c) f_{S|R,C}(s|r,c)\, ds. \tag{2}$$

Observe that $f_{Q|S,C}$ is the streamflow reconstruction from the MADA, and $f_{S|R,C}$ is the MADA reconstruction from tree rings. Thus we have established mathematically the reasoning that tree-ring-based streamflow reconstruction is possible based on the link through soil moisture. $f_{Q|R,C}$ is the marginal distribution without observing the soil moisture. Instead of constructing $f_{Q|R,C}$, we can infer S from R, then Q from S, by constructing $f_{S|R,C}$ and $f_{Q|S,C}$.

3.1.3 Computational advantages of using the MADA, and caveats

The construction of the MADA can be thought of as a transformation from the tree ring network, irregular in both space and time, to a regular grid with homogeneous temporal coverage—analogous to transforming meteorological station data to gridded temperature and precipitation products. This transformation brings several advantages to reconstructing streamflow using the MADA, compared to using the underlying tree ring network.

First, in a typical reconstruction study, one must detrend and standardize the tree ring data to remove non-climate signals (cf. Cook & Kairiukstis, 1990). For a large scale study like ours, such a task is complex. Instead, we can leverage the effort that has been

devoted to detrending and standardizing the chronologies in making the MADA, and use the MADA as proxy, having built the physical and statistical foundations to do so.

Second, the tree ring sites often cluster, with vast empty space between clusters (see e.g. Cook et al. (2010), Figure 1). When taking a subset of them for reconstruction at a station, there can be cases where none or very few sites are within a search radius. The MADA helps "bridging" the space, bringing climate signals from further-away tree sites to grid points nearer to the station. The high resolution grid ($1^\circ \times 1^\circ$ for version 2) makes automated grid point selection easier. (The automated grid point selection procedure is described in Section 3.2.1.)

Third, when reconstructing streamflow from tree rings, nested models are often necessary because tree ring chronologies have different time spans. One starts with the shortest nest, using the common time span of all chronologies to build a model, then dropping the shortest chronology to build a second model with longer time span but less explained variance than the first, and repeating the process, dropping more chronologies to achieve longer time spans until the final nest with the longest time span, but with the lowest explained variance. The nests' outputs are then corrected for their variance and averaged to obtain the final reconstruction (see e.g. D'Arrigo et al., 2011). This nesting step was carried out for the MADA, such that most grid points have the same time span (Figure S4). This lets us use a single common period (1200-2012), and eliminates our need to build nested models back in time. This is particularly desirable for our dynamic state-space reconstruction model, as averaging the nests breaks the link between the catchment state and streamflow. (The reconstruction model is described in Section 3.2.2.)

The computational advantages of using the MADA are thus threefold: (1) no detrending and standardization, (2) easier grid point selection, and (3) no nesting. However, these come with some costs, the most important of which is uncertainty. When reconstructing streamflow from the MADA, we treat the MADA (i.e., the model input) as constant. But in fact, the MADA is a regression product and has its own uncertainty. Furthermore, this uncertainty increases back in time as the number of available chronologies decreases. One way to quantify the uncertainty is by bootstrapping: streamflow reconstructions can be built using bootstrap replicates of the MADA, and the range of the bootstrap ensemble indicates the uncertainty of the reconstruction. An appropriate bootstrapping scheme must be considered, given that the uncertainty is nonstationary, and that dimensionality is a challenge: the MADA has 813 years $\times$ 2716 grid points. In this regard, the added benefit of our reconstruction framework is that it runs for each station individually (see Section 3.2), so one need not reconstruct the whole network in order to quantify uncertainties at specific stations of interest.

As a gridded regression product, the MADA smooths out local variability. This can be alleviated by carefully selecting and processing the grid points to retain as much variance as possible (Section 3.2.1), and by using sufficiently large catchments (Section 2.1).

Finally, we note that the computational advantages we described here are only applicable to large-scale studies, where an automated framework is needed. For individ-

ual sites, we urge researchers to consider all available proxies, rather than being attracted by the convenience offered by the drought atlases.

3.2 Point-by-Point, Climate-informed, Dynamic Streamflow Reconstruction

When reconstructing a climate field, such as a PDSI grid or a streamflow station network, it is desirable to preserve the field covariance structure. However, building a large-scale spatial regression model is challenging. Instead, one can reconstruct each point in the field independently, and rely on the proxy network to capture the spatial patterns. This is the premise of the Point-by-Point Regression (PPR) method (Cook et al., 1999), which has been used to reconstruct drought atlases of Europe (Cook et al., 2015, 2020), the Americas (Cook et al., 1999; Stahle et al., 2016; Morales et al., 2020), Oceania (J. G. Palmer et al., 2015), and Asia (Cook et al., 2010). These drought atlases demonstrate that PPR captures well the spatial patterns of climate variability (see e.g. Cook et al. (1999), Figures 8 and 9). Like these drought atlases, our streamflow network covers a large spatial domain with varying climates; therefore, we adopted the PPR principle, and reconstructed our stations individually. While some aspects of our reconstruction framework followed the PPR procedure, we have innovated many steps of the workflow.

Overall, the framework involves three main stages: (1) input selection (Section 3.2.1), (2) model calibration (Section 3.2.2), and (3) cross-validation (Section 3.2.3). In Stage 1, we selected a subregion of the MADA that is hydroclimatically similar to the streamflow station of interest, and extracted from this subregion a parsimonious subset of principal components, using weighted Principal Component Analysis (PCA). This stage involves two tuning parameters: the hydroclimate similarity threshold, and the PCA weight. For each combination of these parameters, we calibrated a reconstruction model in Stage 2, thus producing an ensemble of models. Finally, in Stage 3, we cross-validated the models to choose the best one, and used that for the final reconstruction.

3.2.1 Climate-informed Input Selection

A regional paleoclimate proxy record, such as the MADA or its underlying tree ring network, is rich with information, but not all of such information is relevant to the streamflow target. A proper input selection is necessary to filter noise and retain only the most relevant signal. A common way is to use proxy sites within a search radius; and PPR does the same. But, given that geographical proximity does not necessarily imply hydroclimatic similarity, we selected our proxies (MADA grid points) by hydroclimatic similarity directly. The hydroclimate at location i (a MADA grid point or a streamflow station) is characterized by three indices: aridity a_i, moisture seasonality s_i, and snow fraction f_i, following Knoben, Woods, and Freer, who proposed this hydroclimate characterization and calculated the indices for a global $0.5° \times 0.5°$ grid (Knoben et al., 2018). The hydroclimatic similarity between two locations i and j is then defined as their Euclidean distance in the hydroclimate space. This distance is termed the KWF distance

and its mathematical definition is

$$d_{KWF}(i,j) = \sqrt{(a_i - a_j)^2 + (s_i - s_j)^2 + (f_i - f_j)^2}. \quad (3)$$

By calculating the KWF distance between each MADA grid point and each streamflow station, we can screen out MADA grid points that are geographically close to the station of interest but hydroclimatically different—a climate-informed grid point selection scheme. Whereas previous PPR implementations varied the search radius, we fixed the radius to 2,500 km—the scale of regional weather systems (Boers et al., 2019)—and varied the KWF distance between 0.1 and 0.3 in 0.05 increments. For reference, the maximum KWF distance between any two points in Monsoon Asia is 1.424. Each KWF distance yielded a search region encompassing a set of MADA grid points surrounding the streamflow station of interest. In our search regions, PDSI often correlates significantly and positively with streamflow (Figure 3); indeed hydroclimatic similarity is a physical basis for correlation.

Next, we performed weighted PCA to remove multicollinearity among the MADA grid points. Following PPR, we weighted each grid point by its correlation with the target streamflow, using equation (4):

$$z_i = g_i r_i^p. \quad (4)$$

Here, g_i is grid point i's scPDSI time series, r_i the correlation between g_i and the target streamflow, p the weight exponent, and z_i the weighted version of g_i. We used $p = 0, 0.5, 2/3, 1, 1.5$, and 2, the same as those used by Cook et al. (2010). We then performed PCA on z_i's, and retained only those principal components (PCs) having eigenvalue at least 1.0 (Hidalgo et al., 2000). From the retained PCs (typically about 20–40 per station), we selected a parsimonious subset that is most relevant to the streamflow target using the VSURF (Variable Selection Using Random Forest) algorithm (Genuer et al., 2010). So, for each combination of KWF distance and PCA weight, we arrived at a subset of PCs for reconstruction. Each streamflow station has an ensemble of 30 such subsets, the best of which was identified using cross-validation (Section 3.2.3) and used for the final reconstruction.

3.2.2 Linear Dynamical System

Having obtained the climatic inputs, the next step was to model the relationship between these inputs and the catchment output (streamflow). Here, this relationship was not modeled with linear regression (as with original PPR, and as typical with previous reconstruction studies), but as a linear dynamical system (LDS), following equations (5) and (6):

$$x_{t+1} = Ax_t + Bu_t + w_t \quad (5)$$

$$y_t = Cx_t + Du_t + v_t \quad (6)$$

where t is the time step (year), y the catchment output (streamflow), u the climatic input (an ensemble member from the climate-informed grid point selection), w and v white noise, and x the hidden system state, which can be interpreted as the catchment's flow

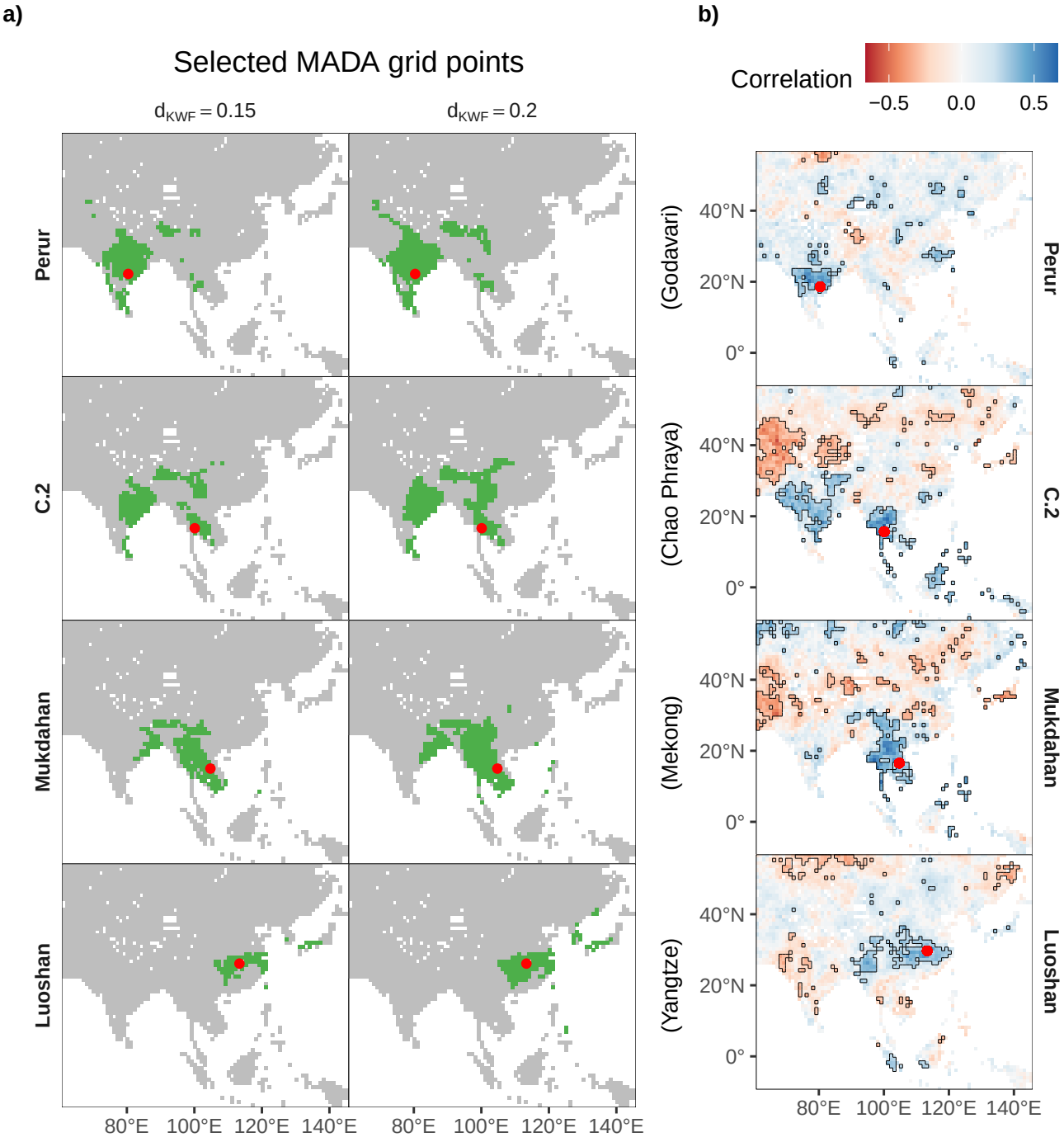

Figure 3. a) Examples of the climate-informed grid point selection: selected MADA grid points (green) based on two KWF distances (columns) at four stations (rows). b) Correlations between streamflow at the same four stations and the MADA, significant correlations ($\alpha = 0.05$) enclosed in black boundaries. The selection regions in (a) generally have significant positive correlation with streamflow. The areas with significant negative correlations need further investigation.

regime, i.e, wet or dry (Nguyen & Galelli, 2018). By modeling the flow regime and its transition, the LDS model accounts for both regime shifts (Turner & Galelli, 2016) and catchment memory (Pelletier & Turcotte, 1997). These behaviors are not modeled in linear regression.

The LDS model assumes that the initial state and the noise processes are normally distributed:

$$w_t \sim \mathcal{N}(0, Q) \tag{7}$$

$$v_t \sim \mathcal{N}(0, R) \tag{8}$$

$$x_1 \sim \mathcal{N}(\mu_1, V_1). \tag{9}$$

It follows that the catchment state and output are also normally distributed. But some of our streamflow records are skewed. These were log-transformed to reduce skewness (Text S3 and Figure S3).

The LDS model is trained using a variant of the Expectation-Maximization algorithm. In the E-step, we fix the model parameters and learn the hidden state. In the M-step, we fix the hidden state and learn the model parameters. Iterations are repeated between the E- and M-steps until convergence. The reconstruction algorithm is implemented in the R package *ldsr* (Nguyen, 2020).

3.2.3 Cross-validation

Consistent with the literature, we assessed reconstruction performance using the metrics Reduction of Error (RE) and Nash-Sutcliffe Coefficient of Efficiency (CE or NSE) (Nash & Sutcliffe, 1970; Fritts, 1976). Mathematically,

$$RE = 1 - \frac{\sum_{t \in \mathcal{V}} (Q_t - \hat{Q}_t)^2}{\sum_{t \in \mathcal{V}} (Q_t - \bar{Q}_c)^2} \tag{10}$$

$$CE = 1 - \frac{\sum_{t \in \mathcal{V}} (Q_t - \hat{Q}_t)^2}{\sum_{t \in \mathcal{V}} (Q_t - \bar{Q}_v)^2} \tag{11}$$

where t is the time step, $\mathcal{V}$ the validation set, Q the observed streamflow, $\hat{Q}$ the reconstructed streamflow, $\bar{Q}_c$ the calibration period mean, and $\bar{Q}_v$ the verification period mean.

Both RE and CE are based on squared error; they can be sensitive to outliers, especially the CE. To address this limitation, Gupta et al. (2009) proposed another metric, which assesses a model output based on its correlation with observation, as well as its bias and variability (equation (12)):

$$KGE = 1 - \sqrt{(\rho - 1)^2 + \left(\frac{\hat{\mu}}{\mu} - 1\right)^2 + \left(\frac{\hat{\sigma}}{\sigma} - 1\right)^2}. \tag{12}$$

Here, ρ is the correlation between model output and observation, $\hat{\mu}$ and μ the modeled and observed mean of the streamflow time series, and $\hat{\sigma}$ and σ the modeled and observed

standard deviation of the streamflow time series. This metric is now known as the Kling-Gupta Efficiency (KGE). The KGE complements RE and CE, and we included the KGE in model assessment.

Conventionally, reconstruction skills are often calculated in a split-sample (i.e., two-fold) cross-validation scheme: the model is calibrated with the first half of the data and validated with the second half, then calibrated with the second half and validated with the first half (see e.g. D'Arrigo et al., 2011). The contiguous halves aim to test a model's ability to capture a regime shift (Briffa et al., 1988). Unfortunately, this scheme is not practical for many stations in our record, where it would leave us only 20–25 data points for calibration (Figure S2). In addition, a two-fold cross-validation scheme provides only two point estimates for each skill score, and they may be notably different (for example, D'Arrigo et al. (2011) reported CE values of 0.21 and 0.73 for the two folds.) As a result, the mean skill score may not be robust. A number of recent works have instead used the leave-k-out cross-validation scheme (e.g., Gallant & Gergis, 2011; Ho et al., 2016; Li et al., 2019). In this scheme, a random chunk of k data points is withheld for validation while the model is calibrated with the remaining data points, then calibration and validation are repeated over as many as 100 chunks of k. This scheme provides a more robust estimate of the mean skill score, but it may not correctly assess the model's ability to capture a regime shift, because the withheld points are not contiguous like in the split-sample scheme.

We sought a balanced approach. In each cross-validation run for each station, we withheld a *contiguous* chunk of 25% of the data points for validation and trained the model on the remaining 75%. This way, we maintain the goal of the split-sample scheme while still having enough data for calibration and getting distributions of skill scores, which yield a reasonably robust mean skill estimate for each metric. Having distributions of skill scores has another benefit: we can now make probabilistic statements about skill. For example, we can calculate the probability that $CE < 0$, and if that probability is less than a threshold α, say 0.1, then we consider the reconstruction statistically skillful with respect to CE at $\alpha = 0.1$. While not doing formal statistical tests, we can make analogous statements about the significance of the skills scores.

When the hold-out chunks are contiguous, there are not as many chunks as when they are random, so we repeated the procedure 30 times instead of 100, and calculated the mean RE, CE and KGE over these 30 runs. When calculating the mean scores, we used the Tukey's biweight robust mean (Mosteller & Tukey, 1977) instead of the arithmetic mean, to limit the effect of outliers. The robust mean is commonly used by dendrochronologists to derive the mean chronology from tree ring samples (Cook & Kairiukstis, 1990), and we have extended its use here. After cross-validating all ensemble members (Section 3.2.1), we selected one member for each station based on the robust mean CE and KGE (RE is similar to CE and is omitted). The ideal score for both CE and KGE is 1; therefore, we calculated for each ensemble member the Euclidean distance between the tuple (CE, KGE) and the point (1, 1). For each station, the ensemble member nearest to the ideal score was used for the final reconstruction.

4 Results and Discussion

4.1 Reconstruction Skills

Reduction of Error (RE) is positive at all stations (Figure 4a and b); Coefficient of Efficiency (CE) is positive at all but one: Kachora in the Indus (Pakistan), where $CE \approx -0.06$ (Figures 4c and d). At $\alpha = 0.1$, 30 stations are statistically skillful with respect to RE, and 23 are with CE (Figure S9). Comparing the histograms of RE and CE (Figures 4b and d), we observe that CE is slightly lower—this is expected as CE is a more stringent metric than RE (Cook & Kairiukstis, 1990). Much lower CE than RE implies overfitting; we do not observe that here.

When using the Kling-Gupta Efficiency (KGE), if one wishes to benchmark a model against the verification period mean (as is with the CE), the threshold value is $1-\sqrt{2} \approx -0.41$, i.e, $KGE > -0.41$ is analogous to $CE > 0$ (Knoben et al., 2019). Our KGE ranges from 0.22 to 0.68 (Figure 4e and f), far higher than the threshold. Furthermore, all 62 stations are statistically skillful with respect to KGE at $\alpha = 0.1$ (Figure S9). These results indicate that our reconstruction model performs well in terms of key characteristics: correlation, bias, and variability.

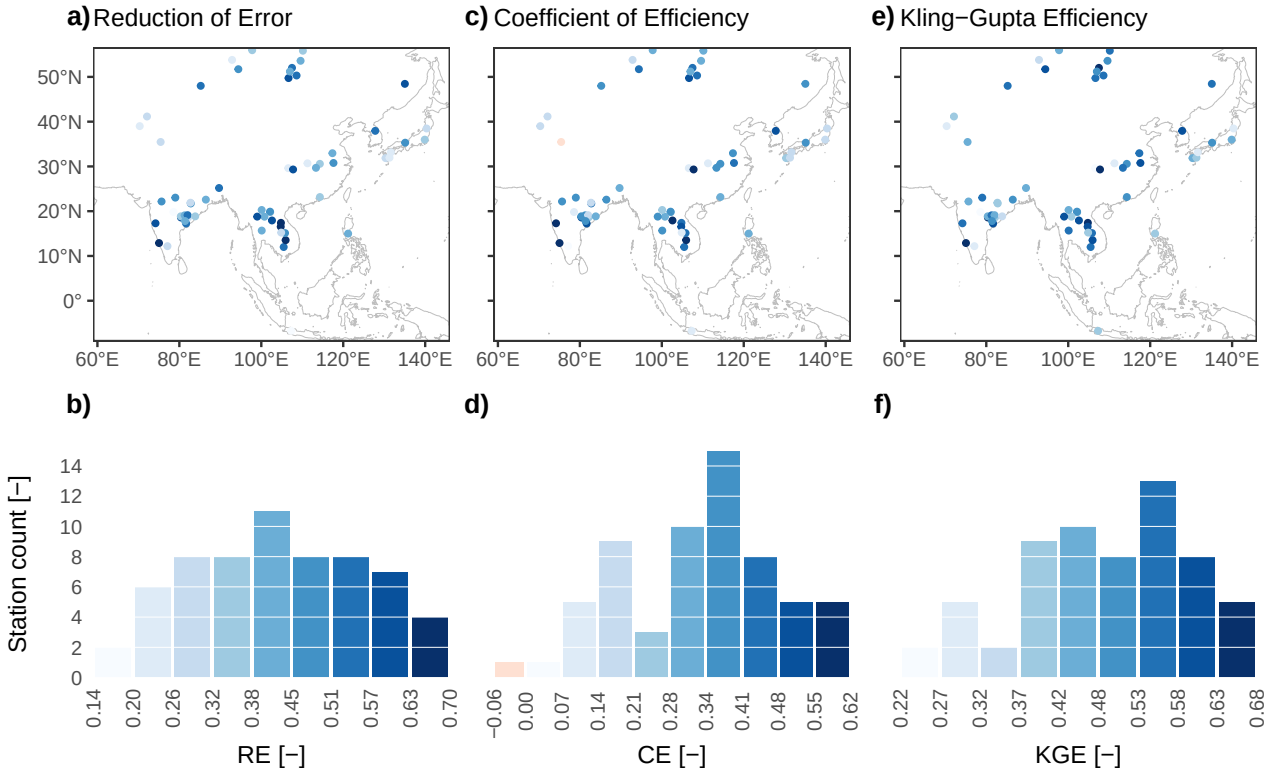

Figure 4. Distribution of model performance scores. Panels a, c, and e show the scores of each station following the color legends encoded with the histograms in panels b, d, and f.

All three metrics have similar spatial distributions (Figure 4a, c, and e). As expected, lower skills are seen in most of Central Asia, Japan, and West Asia, which lie outside the core monsoon area. An exception is the upper reach of the Selenge River, upstream of Lake Baikal, where model skill is high, owing to high quality tree ring records from Mongolia (Davi et al., 2006; Pederson et al., 2013; Davi et al., 2013; Pederson et al., 2014). In all other regions, model skill is homogeneous. The consistent performance of our model suggests that the MADA is a good proxy for streamflow reconstruction in Asia, and our climate-informed dynamic reconstruction is skillful. More validation exercises (Figures S5 to S8) further support the reliability of the reconstruction.

4.2 Spatiotemporal Variability of Monsoon Asia's Streamflow

Having obtained reliable skill scores, we now present eight centuries of spatiotemporal streamflow variability in Monsoon Asia, in terms of standardized streamflow (z-score of mean annual flow) (Figure 5a). This reconstructed history captures the riparian footprint of major historical events—large volcanic eruptions and megadroughts (Figure 5b). We first discuss the impact of the three largest eruptions of the past eight centuries (Sigl et al., 2015): Samalas (1257) (Lavigne et al., 2013), Kuwae (1452-53) (Gao et al., 2006), and Tambora (1815) (Stothers, 1984).

Assuming that Kuwae erupted in 1452 (consistent with tree ring records, see e.g. Briffa et al. (1998)), these three eruptions saw similar streamflow patterns (Figure 5b, panels 1, 4, and 8). In the eruption year t ($t = 1257, 1452, 1815$), large positive streamflow anomalies were observed in Southeast and East Asia. The magnitude of the positive anomalies were largest with Samalas, followed by Kuwae, and then Tambora. The global radiative forcings of the Samalas, Kuwae, and Tambora events are -32.8, -20.5, and -17.1 W/m^2, respectively (Sigl et al., 2015). Thus, we observe a correspondence between the magnitude of positive streamflow anomalies and the magnitude of radiative forcings. This correspondence is also seen clearly from the distributions of streamflow anomalies in the three events (Figure S10a). These results suggest an influence of volcanic eruptions on streamflow in Southeast and East Asia.

Unlike East and Southeast Asia, South Asia's streamflow remained around the normal level in years t and t+1 in all three eruptions, suggesting little volcanic influence. More patterns were also observed: mixed wet and dry conditions in Central Asia, and normal to wet conditions in eastern China and West Asia (cf. Figure S10a). Thus, the influence of volcanic eruptions on Monsoon Asia's streamflow varies spatially, ranging from strong positive, mixed, to little. The mechanisms underlying this spatial variability are yet to be elucidated.

Our results are mostly consistent with Anchukaitis et al. (2010), who used Superposed Epoch Analysis to analyze PDSI anomalies in the eruption years. The key difference is in eastern China, where Anchukaitis et al. (2010) showed negative PDSI in year t, while we observed normal to positive streamflow anomalies in year t, and negative streamflow anomalies in year $t + 1$ (see also Figure S10b). The discrepancies may be due to the different eruption data sets (Anchukaitis et al. (2010) demonstrated this with three

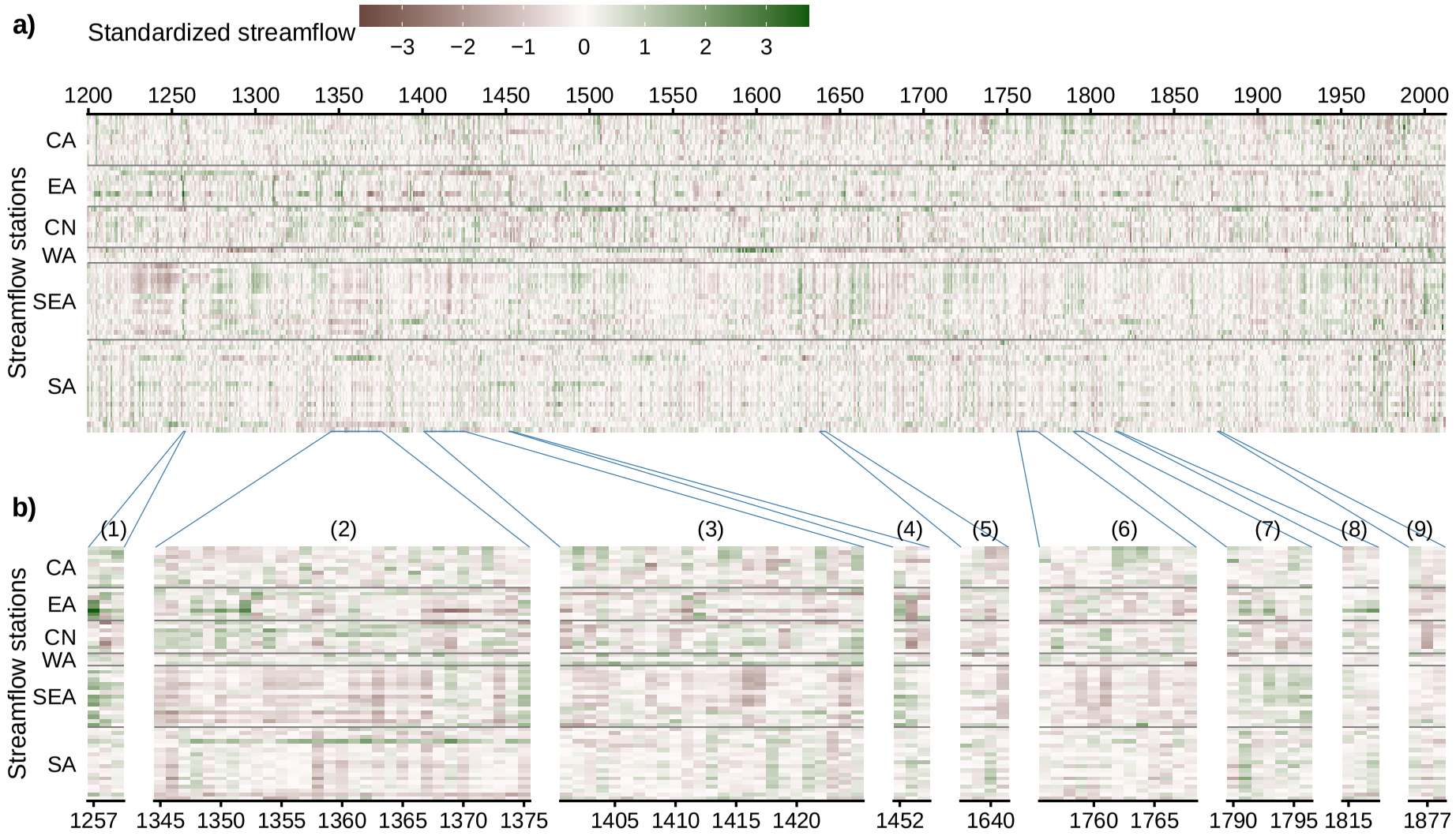

Figure 5. Spatiotemporal variability of streamflow in Monsoon Asia. a) Variations over time (x-axis) and space (y-axis) of the standardized streamflow index (i.e., z-score of streamflow, or z-score of log-transformed streamflow when log-transformation was used in the reconstruction). The stations are arranged approximately north to south (top down on y-axis) and divided into five regions as delineated in Figure 1: CA (Central Asia), EA (East Asia), WA (West Asia), CN (eastern China), SEA (Southeast Asia), and SA (South Asia). b) Historic events captured in the reconstruction: (1) Samalas eruption, (2) and (3) Angkor Droughts I and II, (4) Kuwae eruption, (5) Ming Dynasty Drought, (6) Strange Parallels Drought, (7) East India Drought, (8) Tambora eruption, and (9) Victorian Great Drought.

sets of events) and the analytical methods. It could also be because they analyzed PDSI while we analyzed streamflow. That we observed negative streamflow anomalies in year $t+1$ instead of t could be due to the lagged response of streamflow in this region.

As a drought/pluvial indicator, streamflow may differ from PDSI in individual years for some regions, as discussed above, but on longer terms, our reconstructed streamflow agrees well with reconstructed PDSI. For example, our record fully captures the Angkor Droughts (1345–1374 and 1401–1425) (Buckley et al., 2010, 2014) with prolonged low flow throughout Southeast Asia, and extended as far as India (Figure 5b, panels 2 and 3), in agreement with speleothem records from Dandak and Jhuma Caves (Sinha et al., 2007, 2011). Heavy monsoon rain interrupted these megadroughts; such abrupt alterations to the flow regime proved difficult for the ancient city of Angkor (Buckley et al., 2014). The city once thrived thanks to an extensive network of hydraulic infrastructure (Lieberman & Buckley, 2012). After the first Angkor Drought, the inflow/outflow functions of the *barays* (reservoirs) were altered in an attempt to preserve water. Heavy rains and flooding subsequently destroyed the reduced-capacity hydraulic infrastructure. This flood likely occurred in 1375 (Figure 5b, event 2). By the second Angkor Drought, the "hydraulic city" (Groslier, 1979; Lustig & Pottier, 2007) had insufficient water storage and could not recover.

Four more megadroughts that severely affected Asian societies (Cook et al., 2010) are also captured in our reconstruction (Figure 5b, panels 5, 6, 7, and 9), along with other major droughts and pluvials. For example, Central Asia observed a six-decade drought between 1260–1320, and sustained pluvials during 1740–1769. Most notably, Southeast Asia suffered a drought between 1225–1255 that was comparable in length to Angkor Drought I, but more severe in magnitude. Following this drought was a multi-decadal pluvial in 1271–1307. The drought is prominent in the speleothem record of J. K. Wang et al. (2019), and the pluvial can also be traced from there.

4.3 Links to Oceanic Drivers

To exemplify the spatial variation of how the oceans influence streamflow, we selected four river basins from west to east: Godavari, Chao Phraya, Mekong, and Yangtze, and selected one station from each basin. The selected stations are in the main stream and their reconstructions are statistically skillful.

We calculated the correlation between reconstructed annual streamflow at each station and the seasonal averages of global sea surface temperature (SST) for the period 1856–2012. The season definitions are: December to February (DJF), March to May (MAM), June to August (JJA), and September to November (SON). We also included JJA and SON of the prior year (JJA (-1) and SON (-1)). Correlation patterns vary both seasonally and spatially, with differences among rivers and among oceans (Figure 6).

4.3.1 Pacific Ocean

Tropical Pacific SST correlates significantly with streamflow at all four basins, but the correlation patterns vary. For the Godavari, moderate positive correlations are seen from JJA (−1) to DJF, and strong negative correlations are seen from JJA to SON. For the Yangtze, the pattern is completely opposite: strong positive correlations from JJA (−1) to DJF, and moderate negative correlations in JJA and SON. The location of the strongest correlations suggests links to the El Niño-Southern Oscillation (ENSO, cf. McPhaden et al. (2006)). We find it interesting that ENSO seems to influence the Godavari and Yangtze in contrasting ways.

Unlike the Godavari and Yangtze, the Chao Phraya and Mekong's streamflow correlates significantly with SST over most of the Pacific Ocean, and the correlation persists across all seasons. The correlation pattern is negative in the tropical Pacific, and positive in the northern and southern Pacific. This pattern and its lack of seasonality suggest that, beside ENSO, there are influences from a driver at longer time scales, likely the Pacific Decadal Variability (PDV)—decadal variations of Pacific SST resulted from complex tropical-extratropical ocean-atmosphere interactions (Henley, 2017). The North Pacific component of PDV is known as the Pacific Decadal Oscillation (PDO) (Mantua & Hare, 2002), its southern counterpart the South Pacific Decadal Oscillation (Shakun & Shaman, 2009); basin-wide SST variation patterns have also been termed Interdecadal Pacific Oscillation (Folland et al., 1999). These modes are closely related (Henley, 2017). The PDV has been shown to influence hydroclimatic variability in Monsoon Asia, in conjunction with ENSO (Yu et al., 2018). Specifically for the Chao Phraya, PDV also modulates ENSO's influence on peak flow (Xu et al., 2019).

4.3.2 Indian Ocean

Correlation patterns are less prominent in the Indian Ocean compared to the Pacific. We observe basin-wide correlations in DJF for the Godavari and Yangtze; correlations bear the same sign as that in the Pacific. This is consistent with the Indo-Pacific coupling: an ENSO event in the Pacific leads to SST anomalies of the same sign in the Indian Ocean (Saji et al., 1999). The Godavari and Yangtze also exhibit another correlation pattern in SON (with small areas of significance): correlations bear opposite signs between the tropical western Indian Ocean near the Horn of Africa and the southeastern Indian Ocean around Sumartra. This pattern and its timing suggest links to the Indian Ocean Dipole (IOD) (Saji et al., 1999; Ummenhofer et al., 2017). The IOD accounts for about 12% of Indian Ocean SST variability, much less than the basin-wide coupling mode (30%) (Saji et al., 1999); this explains the weaker correlations of the IOD. Positive IOD events have also been linked to droughts in Southeast Asia, but this relationship is not robust (Ummenhofer et al., 2013). In our analysis, the link between IOD and Southeast Asian streamflow is not visible. Our interpretation is that ENSO and PDV are the main drivers here, and they dominate any links that the IOD might have.

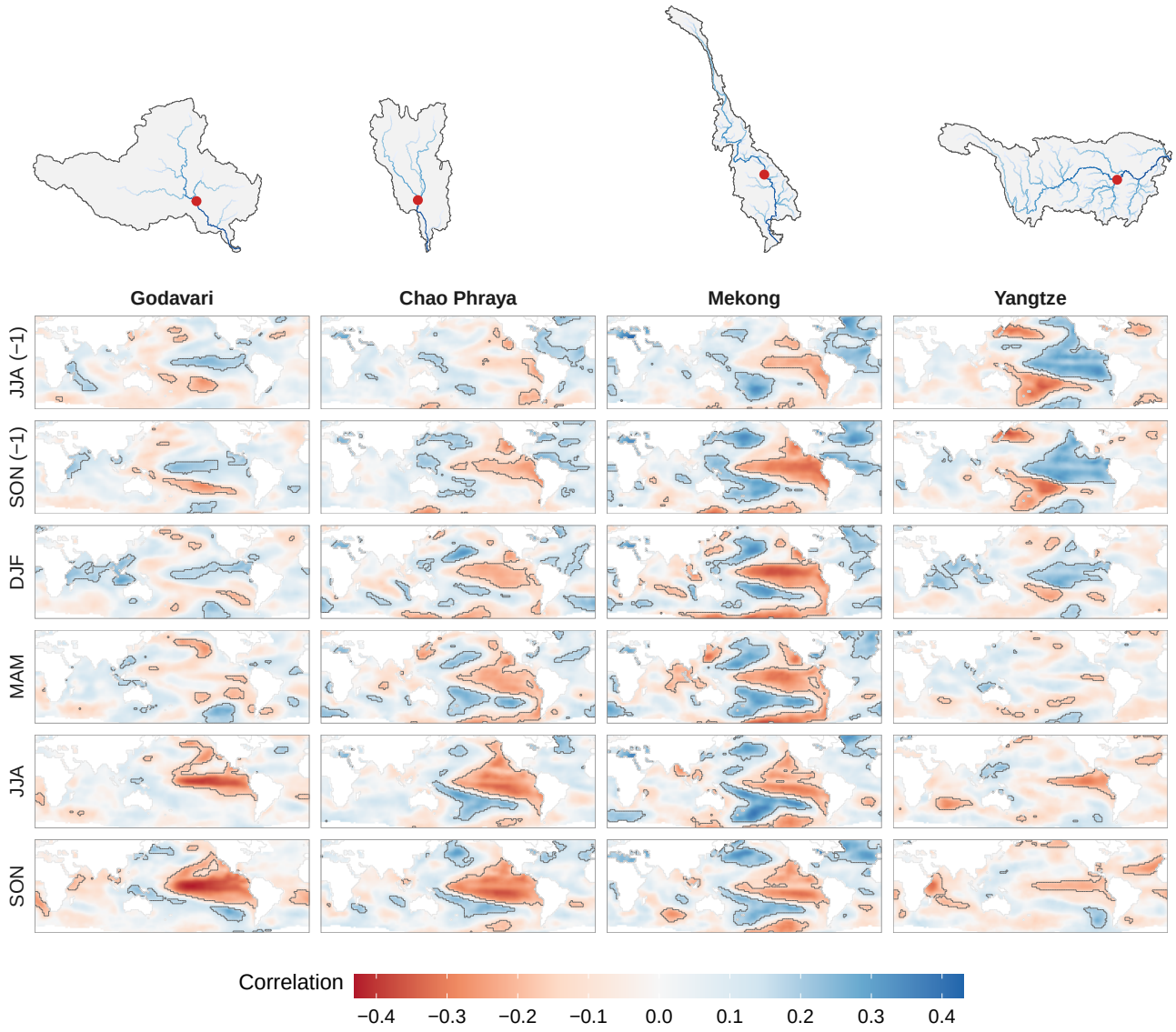

Figure 6. Correlation between reconstructed mean annual streamflow at four river basins (this work) and seasonal averages of global sea surface temperature (SST) from the NOAA_ERSST_v5 data set (Huang et al., 2017) for the period 1856–2012; significant correlations ($\alpha = 0.05$) enclosed in black boundaries. The locations of the stations are shown in the catchment maps; these are the same stations shown in Figure 3. Seasons are marked by the year in which they end. "(-1)" denotes previous year.

4.3.3 Atlantic Ocean

The Chao Phraya and Mekong streamflow correlates positively with tropical and northern Atlantic SST. Significant and consistent correlations are observed throughout the seasons for the Mekong, but less consistent for the Chao Phraya. The link between tropical Atlantic SST and Southeast Asian hydroclimate was also found in a Laotian cave

speleothem record (J. K. Wang et al., 2019). To explain this relationship, J. K. Wang et al. (2019) examined SST, atmospheric pressure, and zonal moisture transport from climate model simulations, and proposed the following mechanism: increased tropical Atlantic SST leads to changes in zonal moisture transport, causing depression over tropical Indian Ocean, reducing rainout over the basin, leaving more moisture available to be transported to mainland Southeast Asia, ultimately strengthening Indian Monsoon rain over the region.

We repeated the correlation analysis above for other stations in the Godavari, Mekong, and Yangtze, where additional stations with statistically skillful results are available on the main stream. Results for those stations are consistent with what we report here (Figures S11 to S13).

4.3.4 Temporal variability of teleconnections

The correlation analysis of Figure 6 shows the spatial variation of the streamflow–SST teleconnection in Monsoon Asia. This analysis was done for the common period of SST and streamflow data (1856–2012). To explore whether and how the teleconnection patterns changed through time, we repeated the correlation analysis using a sliding 50-year window with 10-year increments. We show in Figure 7 three non-overlapping windows, and present all windows in Movie S1. Results show that all correlation patterns changed through time, echoing previous works that found non-stationarities in oceanic teleconnection (e.g., Krishna Kumar et al. (1999); Singhrattna et al. (2005)). Correlations were much weaker in the period 1911–1960 compared to the preceding and subsequent five decades (Figure 7). Some patterns are more transient than others. The Yangtze's JJA-SON pattern of negative correlations with tropical Pacific was only strong in 1921–1980 (Movie S1). On the other hand, the Chao Phraya's SON positive correlations with tropical Pacific persisted throughout all periods. In 1901–1950, when ENSO teleconnection was the weakest for all rivers, tropical and northern Atlantic SST became the strongest teleconnection for the Chao Phraya and Mekong (Movie S1).

5 Conclusions

In this work, we produce the first large-scale and long-term record of streamflow variability for Monsoon Asia, covering 62 stations in 16 countries. In making this record, we also develop a novel automated, climate-informed, and dynamic streamflow reconstruction framework that leverages the computational advantages offered by our climate proxy—the Monsoon Asia Drought Atlas (MADA) version 2. Our framework achieves good skills for most of Monsoon Asia, and skill distribution is spatially homogeneous. Our results provide a regional, synthesized understanding of Monsoon Asia's streamflow variability over the past eight centuries, and reveal how the teleconnection between streamflow and its oceanic drivers varied over space and time.

From our reconstruction, streamflow in Monsoon Asia appears coherent: high and low flows often occur simultaneously at nearby stations and adjacent basins. This co-

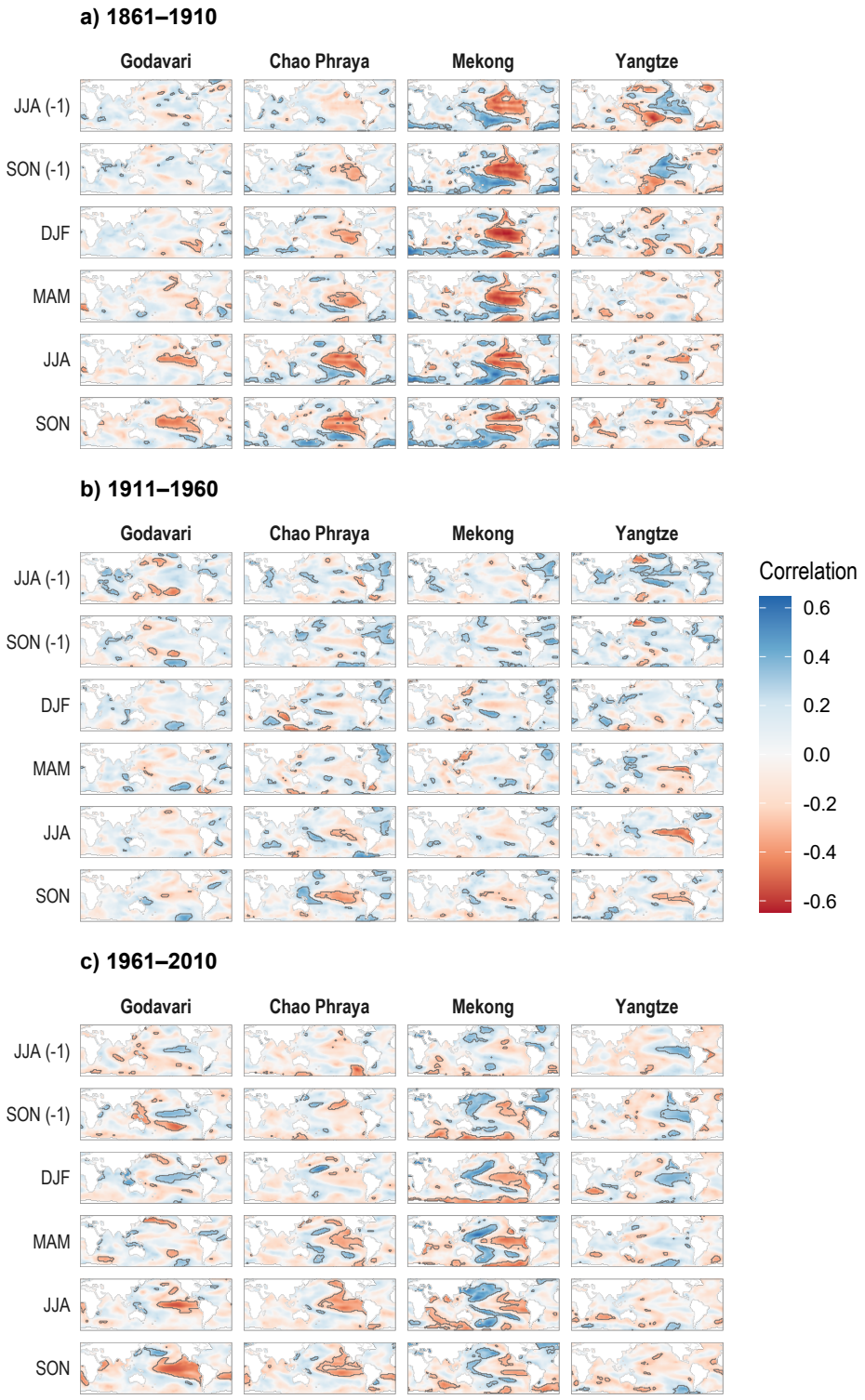

Figure 7. Temporal variability of the streamflow–sea surface temperature correlations. The analysis here is the same as that carried out in Figure 6, but split into three 50-year periods.

herence is attributed to common oceanic drivers—the El Niño–Southern Oscillation (ENSO), the Pacific Decadal Variability (PDV), and sea surface temperature variations in the Indian and Atlantic Oceans. Coherence emerges even though we reconstructed each station individually, demonstrating the merits of Point-by-Point Regression. More importantly, this coherence implies that large-scale infrastructure transferring water, or other water-reliant commodities, across river basins could accidentally expose riparian people to unforeseen risks. For example, Thailand is increasingly purchasing Mekong-generated hydropower from Laos, and when that is insufficient, complements its energy needs with thermal power from plants that use water from the Chao Phraya for cooling. Thailand's energy system is more vulnerable when a prolonged drought occurs at both rivers (Chowdhury et al., 2020)—our record shows such events have happened several times in the past.

We showed that the Pacific, Indian, and Atlantic Oceans influence streamflow variability, and that the strength and spatial footprint of these teleconnections varied over time. This result suggests that our understanding of how water-dependent infrastructure could perform may be narrow, especially in South and Southeast Asia, where we observe alternating periods of strong and weak teleconnections. A narrow characterization of climate-induced risks is likely to misguide climate change assessments, an important source of information for many major infrastructural decisions. Stakes are particularly high in Monsoon Asia, where river basins will experience further pressure in the coming decades (Satoh et al., 2017; Y. Wang et al., 2019). If we can develop methodologies for viewing future changes in streamflow in the context of past and present climate, we then have a pathway for making more informed and robust decisions. The reconstructions developed in our study offer a first step in this direction.

Acknowledgments

Hung Nguyen is supported by the President's Graduate Fellowship from the Singapore University of Technology and Design. We thank Edward Cook, Caroline Ummenhofer, Nerilie Abram, Nathalie Goodkin, Xun Sun, Murray Peel, Rory Nathan, and Robert Wasson for insightful comments. We are indebted to Michelle Ho, Justin Maxwell, Valerie Trouet, two anonymous reviewers, and the Associate Editor for their constructive reviews. We are grateful to Thanh Dang, Mukund Rao, Christoph Libisch-Lehner, Rosanne D'Arrigo, Donghoon Lee, and Caroline Leland for streamflow data of the Mekong, Brahmaputra, Angat, Citarum, Han, and Yeruu Rivers. Chao Phraya River data were obtained from the Thai Royal Irrigation Department at `www.hydro-1.net`, Indus River from Rao et al. (2018, Supporting Information), other streamflow data from GSIM (Do et al., 2018; Gudmundsson et al., 2018), reservoir data from GRanD v1.3 (Lehner et al., 2011), MADA v2 data from Marvel et al. (2019) at `www.dropbox.com/s/n2lo99h9qn17prg/madaV2.nc`, river network data from FLO1K (Barbarossa et al., 2018) with help postprocessing by Valerio Barbarossa, basin boundary data from HydroSHEDS (Lehner & Grill, 2013) at `hydrosheds.org`, SST data from NOAA ERSST v5 (Huang et al., 2017) provided by the NOAA/OAR/ESRL PSD, Boulder, Colorado, USA, at `www.esrl.noaa.gov/psd/`. This work was conducted with open-source software: analysis and visualization performed in R (R Core Team, 2019), maps made in QGIS, and manuscript written in LaTeX. We thank the open-source software community, especially the R package creators and main-

tainers, for their contributions to open science. We provide all data, documented code, and results at `https://github.com/ntthung/paleo-asia` (DOI: `10.5281/zenodo.3818117`); exceptions are instrumental data of the Mekong, Yangtze, and Pearl Rivers due to restrictions. Lamont contribution number XXXX.

References

Adams, K. D., Negrini, R. M., Cook, E. R., & Rajagopal, S. (2015, dec). Annually resolved late Holocene paleohydrology of the southern Sierra Nevada and Tulare Lake, California. *Water Resources Research*, *51*(12), 9708–9724. DOI: 10.1002/2015WR017850

Allen, K. J., Nichols, S. C., Evans, R., Allie, S., Carson, G., Ling, F., ... Baker, P. J. (2017, jan). A 277 year cool season dam inflow reconstruction for Tasmania, southeastern Australia. *Water Resources Research*, *53*(1), 400–414. DOI: 10.1002/2016WR018906

Anchukaitis, K. J., Buckley, B. M., Cook, E. R., Cook, B. I., D'Arrigo, R. D., & Ammann, C. M. (2010). Influence of volcanic eruptions on the climate of the Asian monsoon region. *Geophysical Research Letters*, *37*(22), 1–5. DOI: 10.1029/2010GL044843

Barbarossa, V., Huijbregts, M. A., Beusen, A. H., Beck, H. E., King, H., & Schipper, A. M. (2018, mar). FLO1K, global maps of mean, maximum and minimum annual streamflow at 1 km resolution from 1960 through 2015. *Scientific Data*, *5*(October 2017), 180052. DOI: 10.1038/sdata.2018.52

Best, J. (2019). Anthropogenic stresses on the world's big rivers. *Nature Geoscience*, *12*(1), 7–21. DOI: 10.1038/s41561-018-0262-x

Boers, N., Goswami, B., Rheinwalt, A., Bookhagen, B., Hoskins, B., & Kurths, J. (2019, jan). Complex networks reveal global pattern of extreme-rainfall teleconnections. *Nature*. DOI: 10.1038/s41586-018-0872-x

Briffa, K. R., Jones, P. D., Pilcher, J. R., & Hughes, M. K. (1988, nov). Reconstructing Summer Temperatures in Northern Fennoscandinavia Back to A.D. 1700 Using Tree-Ring Data from Scots Pine. *Arctic and Alpine Research*, *20*(4), 385. DOI: 10.2307/1551336

Briffa, K. R., Jones', P. D., Schweingruber, F. H., & Osborn, T. J. (1998). Influence of volcanic eruptions on Northern Hemisphere summer temperature over the past 600 years. *Nature*, *393*(6684), 450–455. DOI: 10.1038/30943

Buckley, B. M., Anchukaitis, K. J., Penny, D., Fletcher, R., Cook, E. R., Sano, M., ... Hong, T. M. (2010, apr). Climate as a contributing factor in the demise of Angkor, Cambodia. *Proceedings of the National Academy of Sciences*, *107*(15), 6748–6752. DOI: 10.1073/pnas.0910827107

Buckley, B. M., Fletcher, R., Wang, S. Y. S., Zottoli, B., & Pottier, C. (2014). Monsoon extremes and society over the past millennium on mainland Southeast Asia. *Quaternary Science Reviews*, *95*, 1–19. DOI: 10.1016/j.quascirev.2014.04.022

Chen, F., He, Q., Bakytbek, E., Yu, S., & Zhang, R. (2017, nov). Reconstruc-

675 tion of a long streamflow record using tree rings in the upper Kurshab River
676 (Pamir-Alai Mountains) and its application to water resources management.
677 *International Journal of Water Resources Development*, *33*(6), 976–986. DOI:
678 10.1080/07900627.2016.1238347

679 Chen, F., Shang, H., Panyushkina, I., Meko, D., Li, J., Yuan, Y., ... Luo, X. (2019,
680 aug). 500-year tree-ring reconstruction of Salween River streamflow related to
681 the history of water supply in Southeast Asia. *Climate Dynamics*(0123456789).
682 DOI: 10.1007/s00382-019-04948-1

683 Chen, F., Shang, H., Panyushkina, I. P., Meko, D. M., Yu, S., Yuan, Y., & Chen, F.
684 (2019, may). Tree-ring reconstruction of Lhasa River streamflow reveals 472
685 years of hydrologic change on southern Tibetan Plateau. *Journal of Hydrology*,
686 *572*, 169–178. DOI: 10.1016/j.jhydrol.2019.02.054

687 Chen, F., Yuan, Y., Davi, N. K., & Zhang, T. (2016, dec). Upper Irtysh River
688 flow since AD 1500 as reconstructed by tree rings, reveals the hydrocli-
689 matic signal of inner Asia. *Climatic Change*, *139*(3-4), 651–665. DOI:
690 10.1007/s10584-016-1814-y

691 Chen, F., & Yuan, Y.-j. (2016, jul). Streamflow reconstruction for the Guxi-
692 ang River, eastern Tien Shan (China): linkages to the surrounding rivers
693 of Central Asia. *Environmental Earth Sciences*, *75*(13), 1049. DOI:
694 10.1007/s12665-016-5849-1

695 Chen, F., Yuan, Y.-j., Zhang, R.-b., Wang, H.-q., Shang, H.-m., Zhang, T.-w., ...
696 Fan, Z.-a. (2016, jun). Shiyang River streamflow since AD 1765, reconstructed
697 by tree rings, contains far-reaching hydro-climatic signals over and beyond
698 the mid-latitude Asian continent. *Hydrological Processes*, *30*(13), 2211–2222.
699 DOI: 10.1002/hyp.10788

700 Chowdhury, A. F. M., Dang, T. D., Bagchi, A., & Galelli, S. (2020). Expected
701 benefits of Laos' hydropower development curbed by hydro-climatic variability
702 and limited transmission capacity—opportunities to reform. *Journal of Water*
703 *Resources Planning and Management*.

704 Cook, E. R. (2015). *Developing MADAv2 Using The Point-*
705 *By-Point Regression Climate Field Reconstruction Method.*
706 Kyoto, Japan: 4th Asia 2k Workshop. Retrieved from
707 `http://pastglobalchanges.org/download/docs/working{\_}groups/asia2k/4thAsia2k/Cook.ppsx`
708

709 Cook, E. R., Anchukaitis, K. J., Buckley, B. M., D'Arrigo, R. D., Jacoby, G. C.,
710 & Wright, W. E. (2010, apr). Asian Monsoon Failure and Megadrought
711 During the Last Millennium. *Science*, *328*(5977), 486–489. DOI:
712 10.1126/science.1185188

713 Cook, E. R., & Kairiukstis, L. A. (1990). *Methods of dendrochronology. Applications*
714 *in the Environmental Sciences* (E. R. Cook & L. A. Kairiukstis, Eds.). Kluwer
715 Academic Publishers.

716 Cook, E. R., Meko, D. M., Stahle, D. W., & Cleaveland, M. K.
717 (1999). Drought Reconstructuions for the continental United
718 States. *Journal of Climate*, *12*(APRIL), 1145–1162. DOI:

719 10.1175/1520-0442(1999)012⟨1145:DRFTCU⟩2.0.CO;2
720 Cook, E. R., Palmer, J. G., Ahmed, M., Woodhouse, C. A., Fenwick, P., Zafar,
721 M. U., ... Khan, N. (2013). Five centuries of Upper Indus River flow
722 from tree rings. *Journal of Hydrology*, *486*(August 2018), 365–375. DOI:
723 10.1016/j.jhydrol.2013.02.004
724 Cook, E. R., Seager, R., Kushnir, Y., Briffa, K. R., Büntgen, U., Frank, D., ...
725 Zang, C. (2015). Old World megadroughts and pluvials during the Common
726 Era. *Science Advances*, *1*(10), 1–10. DOI: 10.1126/sciadv.1500561
727 Cook, E. R., Solomina, O., Matskovsky, V., Cook, B. I., Agafonov, L., Berd-
728 nikova, A., ... Yermokhin, M. (2020, feb). The European Russia Drought
729 Atlas (1400–2016 CE). *Climate Dynamics*, *54*(3-4), 2317–2335. DOI:
730 10.1007/s00382-019-05115-2
731 Coulthard, B., Smith, D. J., & Meko, D. M. (2016, mar). Is worst-case scenario
732 streamflow drought underestimated in British Columbia? A multi-century per-
733 spective for the south coast, derived from tree-rings. *Journal of Hydrology*,
734 *534*, 205–218. DOI: 10.1016/j.jhydrol.2015.12.030
735 Dai, A., Trenberth, K. E., & Qian, T. (2004). A Global Dataset of Palmer Drought
736 Severity Index for 1870–2002: Relationship with Soil Moisture and Effects
737 of Surface Warming. *Journal of Hydrometeorology*, *5*(6), 1117–1130. DOI:
738 10.1175/JHM-386.1
739 D'Arrigo, R., Abram, N. J., Ummenhofer, C., Palmer, J., & Mudelsee, M. (2011,
740 feb). Reconstructed streamflow for Citarum River, Java, Indonesia: linkages
741 to tropical climate dynamics. *Climate Dynamics*, *36*(3-4), 451–462. DOI:
742 10.1007/s00382-009-0717-2
743 Davi, N. K., Jacoby, G. C., Curtis, A. E., & Baatarbileg, N. (2006). Extension of
744 drought records for central Asia using tree rings: West-central Mongolia. *Jour-
745 nal of Climate*, *19*(1), 288–299. DOI: 10.1175/JCLI3621.1
746 Davi, N. K., Pederson, N., Leland, C., Nachin, B., Suran, B., & Jacoby, G. C.
747 (2013). Is eastern Mongolia drying? A long-term perspective of a mul-
748 tidecadal trend. *Water Resources Research*, *49*(1), 151–158. DOI:
749 10.1029/2012WR011834
750 DeRose, R., Bekker, M. F., Wang, S.-Y., Buckley, B. M., Kjelgren, R., Bardsley,
751 T., ... Allen, E. (2015, oct). A millennium-length reconstruction of Bear
752 River stream flow, Utah. *Journal of Hydrology*, *529*(P2), 524–534. DOI:
753 10.1016/j.jhydrol.2015.01.014
754 Do, H. X., Gudmundsson, L., Leonard, M., & Westra, S. (2018, apr). The Global
755 Streamflow Indices and Metadata Archive (GSIM) – Part 1: The production of
756 a daily streamflow archive and metadata. *Earth System Science Data*, *10*(2),
757 765–785. DOI: 10.5194/essd-10-765-2018
758 Folland, C. K., Parker, D. E., Colman, A. W., & Washington, R. (1999). Large Scale
759 Modes of Ocean Surface Temperature Since the Late Nineteenth Century. In
760 *Beyond el niño* (pp. 73–102). Berlin, Heidelberg: Springer Berlin Heidelberg.
761 DOI: 10.1007/978-3-642-58369-8_4
762 Fritts, H. C. (1976). *Tree Rings and Climate*. London: Elsevier. DOI:

10.1016/B978-0-12-268450-0.X5001-0

Gallant, A. J. E., & Gergis, J. (2011). An experimental streamflow reconstruction for the River Murray, Australia, 1783-1988. *Water Resources Research*, *47*(4), 1–15. DOI: 10.1029/2010WR009832

Gao, C., Robock, A., Self, S., Witter, J. B., Steffenson, J. P., Clausen, H. B., ... Ammann, C. (2006). The 1452 or 1453 A.D. Kuwae eruption signal derived from multiple ice core records: Greatest volcanic sulfate event of the past 700 years. *Journal of Geophysical Research Atmospheres*, *111*(12), 1–11. DOI: 10.1029/2005JD006710

Genuer, R., Poggi, J.-m., & Tuleau-Malot, C. (2010, oct). Variable selection using random forests. *Pattern Recognition Letters*, *31*(14), 2225–2236. DOI: 10.1016/j.patrec.2010.03.014

Gou, X., Chen, F., Cook, E. R., Jacoby, G., Yang, M., & Li, J. (2007). Streamflow variations of the Yellow River over the past 593 years in western China reconstructed from tree rings. *Water Resources Research*, *43*(6), 1–9. DOI: 10.1029/2006WR005705

Gou, X. H., Deng, Y., Chen, F. H., Yang, M. X., Fang, K. Y., Gao, L. L., ... Zhang, F. (2010). Tree ring based streamflow reconstruction for the Upper Yellow River over the past 1234 years. *Chinese Science Bulletin*, *55*(36), 4179–4186. DOI: 10.1007/s11434-010-4215-z

Graham, N. E., & Hughes, M. K. (2007, dec). Reconstructing the Mediaeval low stands of Mono Lake, Sierra Nevada, California, USA. *The Holocene*, *17*(8), 1197–1210. DOI: 10.1177/0959683607085126

Groslier, B. P. (1979). La cité hydraulique angkorienne: exploitation ou surexploitation du sol ? *Bulletin de l'Ecole française d'Extrême-Orient*, *66*(1), 161–202. DOI: 10.3406/befeo.1979.4014

Gudmundsson, L., Do, H. X., Leonard, M., & Westra, S. (2018, apr). The Global Streamflow Indices and Metadata Archive (GSIM) – Part 2: Quality control, time-series indices and homogeneity assessment. *Earth System Science Data*, *10*(2), 787–804. DOI: 10.5194/essd-10-787-2018

Güner, H. T., Köse, N., & Harley, G. L. (2017). A 200-year reconstruction of Kocasu River (Sakarya River Basin, Turkey) streamflow derived from a tree-ring network. *International Journal of Biometeorology*, *61*(3), 427–437. DOI: 10.1007/s00484-016-1223-y

Gupta, H. V., Kling, H., Yilmaz, K. K., & Martinez, G. F. (2009, oct). Decomposition of the mean squared error and NSE performance criteria: Implications for improving hydrological modelling. *Journal of Hydrology*, *377*(1-2), 80–91. DOI: 10.1016/j.jhydrol.2009.08.003

Hart, S. J., Smith, D. J., & Clague, J. J. (2010, sep). A multi-species dendroclimatic reconstruction of Chilko River streamflow, British Columbia, Canada. *Hydrological Processes*, *24*(19), 2752–2761. DOI: 10.1002/hyp.7674

Henley, B. J. (2017). Pacific decadal climate variability: Indices, patterns and tropical-extratropical interactions. *Global and Planetary Change*, *155*(October 2016), 42–55. DOI: 10.1016/j.gloplacha.2017.06.004

Hidalgo, H. G., Piechota, T. C., & Dracup, J. A. (2000, nov). Alternative principal components regression procedures for dendrohydrologic reconstructions. *Water Resources Research*, *36*(11), 3241–3249. DOI: 10.1029/2000WR900097

Hinkley, D. (1977). On Quick Choice of Power Transformation. *Applied Statistics*, *26*(1), 67. DOI: 10.2307/2346869

Ho, M., Lall, U., & Cook, E. R. (2016, jul). Can a paleodrought record be used to reconstruct streamflow?: A case study for the Missouri River Basin. *Water Resources Research*, *52*(7), 5195–5212. DOI: 10.1002/2015WR018444

Ho, M., Lall, U., Sun, X., & Cook, E. R. (2017, apr). Multiscale temporal variability and regional patterns in 555 years of conterminous U.S. streamflow. *Water Resources Research*, *53*(4), 3047–3066. DOI: 10.1002/2016WR019632

Huang, B., Thorne, P. W., Banzon, V. F., Boyer, T., Chepurin, G., Lawrimore, J. H., ... Zhang, H.-M. (2017, oct). Extended Reconstructed Sea Surface Temperature, Version 5 (ERSSTv5): Upgrades, Validations, and Intercomparisons. *Journal of Climate*, *30*(20), 8179–8205. DOI: 10.1175/JCLI-D-16-0836.1

Knoben, W. J. M., Freer, J. E., & Woods, R. A. (2019, oct). Technical note: Inherent benchmark or not? Comparing Nash–Sutcliffe and Kling–Gupta efficiency scores. *Hydrology and Earth System Sciences*, *23*(10), 4323–4331. DOI: 10.5194/hess-23-4323-2019

Knoben, W. J. M., Woods, R. A., & Freer, J. E. (2018). A Quantitative Hydrological Climate Classification Evaluated with Independent Streamflow Data. *Water Resources Research*, *54*(7), 5088–5109. DOI: 10.1029/2018WR022913

Koller, D., & Friedman, N. (2009). *Probabilistic Graphical Models: Principles and Techniques*. MIT Press. Retrieved from `https://books.google.com.sg/books?id=7dzpHCHzNQ4C`

Krishna Kumar, K., Rajagopalan, B., & Cane, M. A. (1999, jun). On the Weakening Relationship Between the Indian Monsoon and ENSO. *Science*, *284*(5423), 2156–2159. DOI: 10.1126/science.284.5423.2156

Lara, A., Bahamondez, A., González-Reyes, A., Muñoz, A. A., Cuq, E., & Ruiz-Gómez, C. (2015). Reconstructing streamflow variation of the Baker River from tree-rings in Northern Patagonia since 1765. *Journal of Hydrology*, *529*(P2), 511–523. DOI: 10.1016/j.jhydrol.2014.12.007

Lavigne, F., Degeai, J. P., Komorowski, J. C., Guillet, S., Robert, V., Lahitte, P., ... De Belizal, E. (2013). Source of the great A.D. 1257 mystery eruption unveiled, Samalas volcano, Rinjani Volcanic Complex, Indonesia. *Proceedings of the National Academy of Sciences of the United States of America*, *110*(42), 16742–16747. DOI: 10.1073/pnas.1307520110

Lehner, B., & Grill, G. (2013, jul). Global river hydrography and network routing: baseline data and new approaches to study the world's large river systems. *Hydrological Processes*, *27*(15), 2171–2186. DOI: 10.1002/hyp.9740

Lehner, B., Liermann, C. R., Revenga, C., Vörösmarty, C., Fekete, B., Crouzet, P., ... Wisser, D. (2011, nov). High-resolution mapping of the world's reservoirs and dams for sustainable river-flow management. *Frontiers in Ecology and the Environment*, *9*(9), 494–502. DOI: 10.1890/100125

Li, J., Shao, X., Qin, N., & Li, Y. (2018, may). Runoff variations at the source of the Yangtze River over the past 639 years based on tree-ring data. *Climate Research*, *75*(2), 131–142. DOI: 10.3354/cr01510

Li, J., Xie, S.-P., Cook, E. R., Chen, F., Shi, J., Zhang, D. D., ... Zhao, Y. (2019, jan). Deciphering Human Contributions to Yellow River Flow Reductions and Downstream Drying Using Centuries-Long Tree Ring Records. *Geophysical Research Letters*, *46*(2), 898–905. DOI: 10.1029/2018GL081090

Libisch-Lehner, C. P., Nguyen, H. T. T., Taormina, R., Nachtnebel, H. P., & Galelli, S. (2019, apr). On the Value of ENSO State for Urban Water Supply System Operators: Opportunities, Trade-Offs, and Challenges. *Water Resources Research*, *55*(4), 2856–2875. DOI: 10.1029/2018WR023622

Lieberman, V., & Buckley, B. (2012). *The impact of climate on Southeast Asia, circa 950-1820: New findings* (Vol. 46) (No. 5). DOI: 10.1017/S0026749X12000091

Liu, Y., Sun, J., Song, H., Cai, Q., Bao, G., & Li, X. (2010, may). Tree-ring hydrologic reconstructions for the Heihe River watershed, western China since AD 1430. *Water Research*, *44*(9), 2781–2792. DOI: 10.1016/J.WATRES.2010.02.013

Lustig, T., & Pottier, C. (2007). *The Angkorian Hydraulic City: Exploitation or Over-Exploitation of the Soil? Translation into English of Groslier , B-P . Le cité hydraulique angkorienne: exploitation ou surexploitation du sol?* (Aséanie 20 ed.; F. Lagirarde, Ed.). Bangkok: EFEO Diffusion, Aséanie Bangkok.

Mantua, N. J., & Hare, S. R. (2002). The Pacific Decadal Oscillation. *Journal of Oceanography*, *58*(1), 35–44. DOI: 10.1023/A:1015820616384

Marvel, K., Cook, B. I., Bonfils, C. J. W., Durack, P. J., Smerdon, J. E., & Williams, A. P. (2019). Twentieth-century hydroclimate changes consistent with human influence. *Nature*, *569*(7754), 59–65. DOI: 10.1038/s41586-019-1149-8

McPhaden, M. J., Zebiak, S. E., & Glantz, M. H. (2006, dec). ENSO as an Integrating Concept in Earth Science. *Science*, *314*(5806), 1740–1745. DOI: 10.1126/science.1132588

Morales, M. S., Cook, E. R., Barichivich, J., Christie, D. A., Villalba, R., LeQuesne, C., ... Boninsegna, J. A. (2020, jul). Six hundred years of South American tree rings reveal an increase in severe hydroclimatic events since mid-20th century. *Proceedings of the National Academy of Sciences*, 202002411. DOI: 10.1073/pnas.2002411117

Mosteller, F., & Tukey, J. W. (1977). *Data Analysis and Regression: a second course in statistics*. Addison-Wesley.

Nash, J. E., & Sutcliffe, J. V. (1970, apr). River flow forecasting through conceptual models part I — A discussion of principles. *Journal of Hydrology*, *10*(3), 282–290. DOI: 10.1016/0022-1694(70)90255-6

Nguyen, H. T. T. (2020). *ldsr: Linear Dynamical System Reconstruction.* Retrieved from `https://cran.r-project.org/package=ldsr`

Nguyen, H. T. T., & Galelli, S. (2018, mar). A Linear Dynamical Systems Ap-

proach to Streamflow Reconstruction Reveals History of Regime Shifts in Northern Thailand. *Water Resources Research*, *54*(3), 2057–2077. DOI: 10.1002/2017WR022114

Palmer, J. G., Cook, E. R., Turney, C. S. M., Allen, K. J., Fenwick, P., Cook, B. I., ... Baker, P. (2015, dec). Drought variability in the eastern Australia and New Zealand summer drought atlas (ANZDA, CE 1500–2012) modulated by the Interdecadal Pacific Oscillation. *Environmental Research Letters*, *10*(12), 124002. DOI: 10.1088/1748-9326/10/12/124002

Palmer, W. C. (1965). *Meteorological Drought. Research Paper No. 45.* U.S. Department of Commerce Weather Bureau.

Panyushkina, I. P., Meko, D. M., Macklin, M. G., Toonen, W. H. J., Mukhamadiev, N. S., Konovalov, V. G., ... Sagitov, A. O. (2018, oct). Runoff variations in Lake Balkhash Basin, Central Asia, 1779–2015, inferred from tree rings. *Climate Dynamics*, *51*(7-8), 3161–3177. DOI: 10.1007/s00382-018-4072-z

Pederson, N., Hessl, A. E., Baatarbileg, N., Anchukaitis, K. J., & Di Cosmo, N. (2014). Pluvials, droughts, the Mongol Empire, and modern Mongolia. *Proceedings of the National Academy of Sciences of the United States of America*, *111*(12), 4375–4379. DOI: 10.1073/pnas.1318677111

Pederson, N., Leland, C., Nachin, B., Hessl, A. E., Bell, A. R., Martin-Benito, D., ... Davi, N. K. (2013). Three centuries of shifting hydroclimatic regimes across the Mongolian Breadbasket. *Agricultural and Forest Meteorology*, *178-179*, 10–20. DOI: 10.1016/j.agrformet.2012.07.003

Pelletier, J. D., & Turcotte, D. L. (1997). Long-range persistence in climatological and hydrological time series: Analysis, modeling and application to drought hazard assessment. *Journal of Hydrology*, *203*(1-4), 198–208. DOI: 10.1016/S0022-1694(97)00102-9

Prairie, J., Nowak, K., Rajagopalan, B., Lall, U., & Fulp, T. (2008). A stochastic nonparametric approach for streamflow generation combining observational and paleoreconstructed data. *Water Resources Research*, *44*(6), 1–11. DOI: 10.1029/2007WR006684

R Core Team. (2019). *R: A Language and Environment for Statistical Computing.* Vienna, Austria. Retrieved from `https://www.r-project.org/`

Rao, M. P., Cook, E. R., Cook, B. I., Palmer, J. G., Uriarte, M., Devineni, N., ... Wahab, M. (2018, aug). Six Centuries of Upper Indus Basin Streamflow Variability and Its Climatic Drivers. *Water Resources Research*, *54*(8), 5687–5701. DOI: 10.1029/2018WR023080

Robeson, S. M., Maxwell, J. T., & Ficklin, D. L. (2020). Bias Correction of Paleoclimatic Reconstructions: A New Look at 1,200+ Years of Upper Colorado River Flow. *Geophysical Research Letters*, *47*(1), 1–12. DOI: 10.1029/2019GL086689

Saji, N. H., Goswami, B. N., Vinayachandran, P. N., & Yamagata, T. (1999, sep). A dipole mode in the tropical Indian Ocean. *Nature*, *401*(6751), 360–363. DOI: 10.1038/43854

Satoh, Y., Kahil, T., Byers, E., Burek, P., Fischer, G., Tramberend, S., ... Wada,

939 Y. (2017, jul). Multi-model and multi-scenario assessments of Asian water
940 futures: The Water Futures and Solutions (WFaS) initiative. *Earth's Future*,
941 *5*(7), 823–852. DOI: 10.1002/2016EF000503
942 Sauchyn, D., & Ilich, N. (2017, nov). Nine Hundred Years of Weekly Streamflows:
943 Stochastic Downscaling of Ensemble Tree-Ring Reconstructions. *Water Re-*
944 *sources Research*, 1–18. DOI: 10.1002/2017WR021585
945 Sauchyn, D., Vanstone, J., St. Jacques, J.-M., & Sauchyn, R. (2015, oct).
946 Dendrohydrology in Canada's western interior and applications to wa-
947 ter resource management. *Journal of Hydrology*, *529*, 548–558. DOI:
948 10.1016/j.jhydrol.2014.11.049
949 Shakun, J. D., & Shaman, J. (2009, oct). Tropical origins of North and South Pa-
950 cific decadal variability. *Geophysical Research Letters*, *36*(19), L19711. DOI:
951 10.1029/2009GL040313
952 Sigl, M., Winstrup, M., McConnell, J. R., Welten, K. C., Plunkett, G., Ludlow,
953 F., ... Woodruff, T. E. (2015). Timing and climate forcing of volcanic
954 eruptions for the past 2,500 years. *Nature*, *523*(7562), 543–549. DOI:
955 10.1038/nature14565
956 Singhrattna, N., Rajagopalan, B., Krishna Kumar, K., & Clark, M. P. (2005). Inter-
957 annual and interdecadal variability of Thailand summer monsoon season. *Jour-*
958 *nal of Climate*, *18*(11), 1697–1708. DOI: 10.1175/JCLI3364.1
959 Sinha, A., Berkelhammer, M., Stott, L., Mudelsee, M., Cheng, H., & Biswas, J.
960 (2011, aug). The leading mode of Indian Summer Monsoon precipitation
961 variability during the last millennium. *Geophysical Research Letters*, *38*(15).
962 DOI: 10.1029/2011GL047713
963 Sinha, A., Cannariato, K. G., Stott, L. D., Cheng, H., Edwards, R. L., Yadava,
964 M. G., ... Singh, I. B. (2007, aug). A 900-year (600 to 1500 A.D.) record
965 of the Indian summer monsoon precipitation from the core monsoon zone of
966 India. *Geophysical Research Letters*, *34*(16). DOI: 10.1029/2007GL030431
967 Stagge, J. H., Rosenberg, D. E., DeRose, R. J., & Rittenour, T. M. (2018). Monthly
968 paleostreamflow reconstruction from annual tree-ring chronologies. *Journal of*
969 *Hydrology*, *557*, 791–804. DOI: 10.1016/j.jhydrol.2017.12.057
970 Stahle, D. W., Cook, E. R., Burnette, D. J., Villanueva, J., Cerano, J., Burns, J. N.,
971 ... Howard, I. M. (2016, oct). The Mexican Drought Atlas: Tree-ring re-
972 constructions of the soil moisture balance during the late pre-Hispanic, colo-
973 nial, and modern eras. *Quaternary Science Reviews*, *149*, 34–60. DOI:
974 10.1016/j.quascirev.2016.06.018
975 Stockton, C., & Jacoby, G. C. (1976). *Long-term Surface-water Supply and Stream-*
976 *flow Trends in the Upper Colorado River Basin Based on Tree-ring Analyses*
977 (Tech. Rep.). Lake Powell Research Project.
978 Stothers, R. B. (1984, jun). The Great Tambora Eruption in 1815 and Its After-
979 math. *Science*, *224*(4654), 1191–1198. DOI: 10.1126/science.224.4654.1191
980 Strange, B. M., Maxwell, J. T., Robeson, S. M., Harley, G. L., Therrell, M. D., &
981 Ficklin, D. L. (2019, jun). Comparing three approaches to reconstructing
982 streamflow using tree rings in the Wabash River basin in the Midwestern, US.

Journal of Hydrology, *573*, 829–840. DOI: 10.1016/j.jhydrol.2019.03.057

Tozer, C. R., Kiem, A. S., Vance, T. R., Roberts, J. L., Curran, M. A. J., & Moy, A. D. (2018). Reconstructing pre-instrumental streamflow in Eastern Australia using a water balance approach. *Journal of Hydrology*, *558*, 632–646. DOI: S0022169418300738

Turner, S. W. D., & Galelli, S. (2016, may). Regime-shifting streamflow processes: Implications for water supply reservoir operations. *Water Resources Research*, *52*(5), 3984–4002. DOI: 10.1002/2015WR017913

Ummenhofer, C. C., Biastoch, A., & Böning, C. W. (2017). Multidecadal indian ocean variability linked to the pacific and implications for preconditioning indian ocean dipole events. *Journal of Climate*, *30*(5), 1739–1751. DOI: 10.1175/JCLI-D-16-0200.1

Ummenhofer, C. C., D'Arrigo, R. D., Anchukaitis, K. J., Buckley, B. M., & Cook, E. R. (2013, mar). Links between Indo-Pacific climate variability and drought in the Monsoon Asia Drought Atlas. *Climate Dynamics*, *40*(5-6), 1319–1334. DOI: 10.1007/s00382-012-1458-1

van der Schrier, G., Barichivich, J., Briffa, K. R., & Jones, P. D. (2013, may). A scPDSI-based global data set of dry and wet spells for 1901-2009. *Journal of Geophysical Research: Atmospheres*, *118*(10), 4025–4048. DOI: 10.1002/jgrd.50355

Wang, J. K., Johnson, K. R., Borsato, A., Amaya, D. J., Griffiths, M. L., Henderson, G. M., ... Mason, A. (2019). Hydroclimatic variability in Southeast Asia over the past two millennia. *Earth and Planetary Science Letters*, *525*, 115737. DOI: 10.1016/j.epsl.2019.115737

Wang, Y., Byers, E., Parkinson, S., Wanders, N., Wada, Y., Mao, J., & Bielicki, J. M. (2019, oct). Vulnerability of existing and planned coal-fired power plants in Developing Asia to changes in climate and water resources. *Energy & Environmental Science*, *12*(10), 3164–3181. DOI: 10.1039/C9EE02058F

Wells, N., Goddard, S., & Hayes, M. J. (2004, jun). A Self-Calibrating Palmer Drought Severity Index. *Journal of Climate*, *17*(12), 2335–2351. DOI: 10.1175/1520-0442(2004)017⟨2335:ASPDSI⟩2.0.CO;2

Woodhouse, C. A., Gray, S. T., & Meko, D. M. (2006). Updated streamflow reconstructions for the Upper Colorado River Basin. *Water Resources Research*, *42*(5), 1–16. DOI: 10.1029/2005WR004455

Xu, C., Buckley, B. M., Promchote, P., Wang, S. S., Pumijumnong, N., An, W., ... Guo, Z. (2019). Increased Variability of Thailand's Chao Phraya River Peak Season Flow and Its Association With ENSO Variability: Evidence From Tree Ring δ 18 O. *Geophysical Research Letters*, *46*(9), 4863–4872. DOI: 10.1029/2018GL081458

Xu, C., Pumijumnong, N., Nakatsuka, T., Sano, M., & Li, Z. (2015). A tree-ring cellulose δ18O-based July-October precipitation reconstruction since AD 1828, northwest Thailand. *Journal of Hydrology*, *529*(P2), 433–441. DOI: 10.1016/j.jhydrol.2015.02.037

Yang, B., Chen, X., He, Y., Wang, J., & Lai, C. (2019). Reconstruction of

annual runoff since CE 1557 using tree-ring chronologies in the upper Lancang-Mekong River basin. *Journal of Hydrology*, *569*, 771–781. DOI: 10.1016/j.jhydrol.2018.12.034

Yang, B., Qin, C., Shi, F., & Sonechkin, D. M. (2012). Tree ring-based annual streamflow reconstruction for the Heihe River in arid northwestern China from ad 575 and its implications for water resource management. *Holocene*, *22*(7), 773–784. DOI: 10.1177/0959683611430411

Yu, E., King, M. P., Sobolowski, S., Otterå, O. H., & Gao, Y. (2018, jun). Asian droughts in the last millennium: a search for robust impacts of Pacific Ocean surface temperature variabilities. *Climate Dynamics*, *50*(11-12), 4671–4689. DOI: 10.1007/s00382-017-3897-1

Yuan, Y., Shao, X., Wei, W., Yu, S., Gong, Y., & Trouet, V. (2007, dec). The Potential to Reconstruct Manasi River Streamflow in the Northern Tien Shan Mountains (NW China). *Tree-Ring Research*, *63*(2), 81–93. DOI: 10.3959/1536-1098-63.2.81

Zhang, D., Zhang, Q., Werner, A. D., & Liu, X. (2016). GRACE-Based Hydrological Drought Evaluation of the Yangtze River Basin, China. *Journal of Hydrometeorology*, *17*(3), 811–828. DOI: 10.1175/JHM-D-15-0084.1

Zhang, T., Yuan, Y., Chen, F., Yu, S., Zhang, R., Qin, L., & Jiang, S. (2018, feb). Reconstruction of hydrological changes based on tree-ring data of the Haba River, northwestern China. *Journal of Arid Land*, *10*(1), 53–67. DOI: 10.1007/s40333-017-0034-2